Measuring the topological charge of vortices with diffraction and interference techniques

Yu. Yu. Choporova[1,2], B. A. Knyazev[1,2], N. D. Osintseva[1,3], V.S. Pavelyev[4]

[1]Budker Institute of Nuclear Physics, Novosibirsk, 63090 Russia
[2]Novosibirsk State University, Novosibirsk, 630090 Russia
[3]Novosibirsk State Technical University, Novosibirsk, 630073 Russia
[4]Samara National Research University, Samara, 443086 Russia

***Abstract* - Vortex Bessel beams with topological charges $l = \pm 1$ and $l = \pm 2$ were generated with diffractive optical elements in the THz range using monochromatic and tunable radiation of the Novosibirsk free electron laser. Diffractive and interference techniques were applied to study the main characteristics of the vortex beams, i.e. topological charge and pitch-factor. Analytical studies, simulations and experimental results are given.**

I. INTRODUCTION

Nowadays beams with orbital angular momentum (OAM) or vortex beams are actively investigated in the THz range [1-3]. Using the radiation of the Novosibirsk free electron laser we were able to generate Bessel beams with OAM at 2.13 THz [4]. Silicon binary spiral phase axicons are used for generating vortex beams with topological charges $l = \pm 1$ and $l = \pm 2$. The main characteristics of vortex beams are the topological charge (the number of times that the phase of the beam passes through the interval $[0, 2\pi]$) and the pitch-factor (distance of a full turn of the wavefront). In this paper we show diffractive and interference techniques to study these properties.

II. RESULTS

To visualize the topological charge, we used two methods: diffraction patterns obtained from Young's double-slit experiment and by interference in a Mach-Zehnder interferometer. For Young's experiment, the phase change along the slits from 0 to $2\pi l$ leads to a dogleg-like diffraction pattern (Fig 1a), which can be described by the equation

$$x(y) = -a\tan\left[\frac{2\pi a y}{lz\lambda} + \frac{m\pi}{l} + \frac{\pi}{2}\right], \quad m = 0\ldots l-1, \quad (2)$$

where a is the half distance between the slits (2.25 mm), and z is the propagation distance which is equal to 140 mm (Fig. 1). Experimental patterns were obtained by a microbolometer array with size 16.32×12.24 mm^2, all simulated images have the same size. The order of diffraction maxima shift is equal to the value of topological charge, and the direction of fringe shift corresponds to the sign of the helicity.

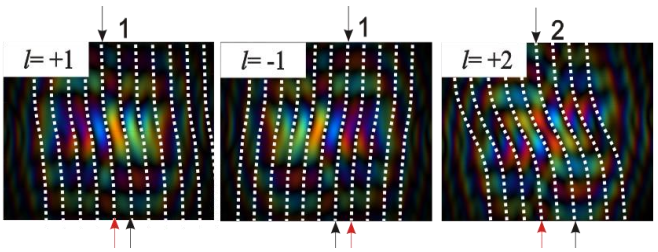

Fig. 1 Simulated diffraction patterns of vortex beams in a double-slit experiment. The color shows phase changes from 0 (blue) to 2π (red). Arrows correspond to the shift value.

Another method to determine the topological charge is to look at the interference between a vortex beam (azimuthally changing phase profile) and a plane wave (constant phase) (Fig. 2). The in-line interference pattern is formed as a constructive and destructive interference along concentric rings. The phase shift of adjacent rings in the interference pattern equals π, according to the distribution of the Bessel function (Fig. 2 left). It can also be seen that, with increasing propagation length, the wavefront becomes spherical (concentric rings become spirals). Since at such a short distance the wavefront of the Gaussian beam remains practically flat, the spiral diffraction patterns observed in the second column of Fig. 2 indicate the appearance of an additional divergence of Bessel beams. This is due to the peculiarity of Bessel beam propagation. The propagation distance is limited by an intersection of conically converging plane waves (diffraction on an axicon). A Bessel beam, formed within the intersection zone, maintains its cross-section within a certain distance. The so-called non-diffractive propagation distance $z_{non\text{-}diff}$ depends on axicon radius r and diffraction angle ϑ:

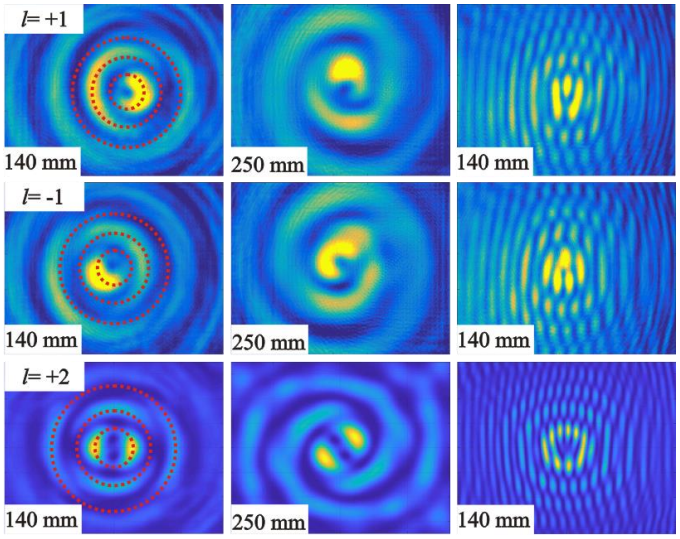

Fig. 2. Experimental (top and middle rows) and simulated (bottom row) in-line and off-axis interference of vortex beams with a Gaussian beam (plane wave) at 140 and 250 mm. All images are 16.32×12.24 mm. Red dotted circular lines correspond to rings of input Bessel beams.

$$z_{non-diff} = \frac{r}{\tan \vartheta}. \quad (1)$$

In our case, the non-diffractive propagation length is about 250 mm (radii of axicons charges $l = \pm 1$ and $l = \pm 2$ is equal to r=30 mm).

In the case of an off-axis interference, the pattern shows a fork dislocation (Fig. 2, the right column). The magnitude of this dislocation is proportional to the topological charge.

The pitch-factors were determined by diffraction on a half-plane (Fig. 3). Simulated diffraction patterns show the rotation of diffraction maxima of each Bessel ring. It follows from the figure that the total rotation distance for $l = +1$ of the first ring is $z_{PitchSim}$= 252 mm from the surface of the axicon, which corresponds to 1.19×10^9 turns per second. The second ring pitch factor is 2042 mm, which corresponds to 0.15×10^9 turns per second. It can be seen in Fig. 3 (the right column) that the inner ring rotates more rapidly than the outer one for the vortex Bessel beam.

Analytically the pitch factor can be calculated by the equation (здесь стоило бы сослаться на оригинальную статью – ссылка есть в PRA)

$$z_{PitchCalc} = \frac{2\pi k \rho^2}{l}, \quad (3)$$

where ρ is radius of the ring. It is worth mentioning that the pitch-factor only takes into account the absolute value of a topological charge, and hence is equal for $l = \pm 1$.

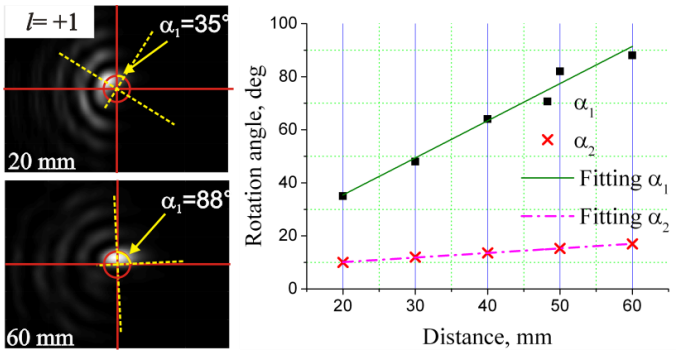

Fig. 3. Simulated diffraction pattern of a vortex beam with $l = +1$ after a half-plane at 20, and 60 mm behind the plane. Dotted curves show the angle of the beam rotation and the distance (left). The dependence of the rotation angle of diffraction maximum of first (α_1) and second (α_2) rings from distance behind the plane (right).

Tab. 1. Parameters of vortex Bessel beams with topological charges 1 and 2

	l=1, 1st ring	l=1, 2nd ring	l=2, 1st ring	l=2, 2nd ring
ρ	0.9 mm	2.8 mm	1.9 mm	4 mm
$z_{PitchCalc}$	227 mm	2195 mm	505 mm	2240 mm

In the case of Bessel beams formed by binary phase axicons with identical periods (это принципиально!), which (whose используется только с одушевленными объектами) electric field can be described by $E(r,\varphi,z) = E_0 J_l(\kappa r)\exp[i(k_z z - l\varphi)]$, rings diameters are not a function of the wavelength and are determined by the topological charge only.

III. Summary

Vortex Bessel beams with orbital angular momentum were generated by silicon binary phase axicons using monochromatic radiation of Novosibirsk FEL. Several diffractive and interferometric techniques were applied for a detailed study of wavefront and topological charge of these beams. The magnitude of the topological charge can be measured inYoung's double-slit experiment and by off-axis interference in a Mach-Zehnder interferometer. In-line interference shows the phase distribution of vortex beam as well as the absolute value of the topological charge. The rotation of the beam was demonstrated in the half-plane diffraction simulation. The methods used to study Bessel beams in the terahertz range can be applied to study vortex beams in other spectral ranges.

IV. Acknowledgments

The simulations were supported by RFBR grant (№ 18-32-00407). The beamline for transport of NovoFEL radiation to the workstation was produced with the support of the Russian Science Foundation (grant 14-50-00080). The Ministry of Education and Science of the Russian Federation supported the collective research center (project RFMEFI62117X0012).

References

[1]. J. He, X Wang, D. Hu, J. Ye, S. Feng, Q. Kan and Y. Zhang, "Generation and evolution of the terahertz vortex beam," *Optics express*, vol. 21(17), pp. 20230-20239, 2013.

[2]. R. Imai, N. Kanda, T. Higuchi, K. Konishi, and M. Kuwata-Gonokami, "Generation of broadband terahertz vortex beams," *Optics letters*, vol. 39(13), pp. 3714-3717, 2014.

[3]. K. Miyamoto, K. Suizu, T. Akiba, and T. Omatsu, "Direct observation of the topological charge of a terahertz vortex beam generated by a Tsurupica spiral phase plate," *Applied Physics Letters*, vol. 104(26), p. 261104, 2014.

[4]. B. A. Knyazev, Y. Y. Choporova, M. S. Mitkov, V. S. Pavelyev, and B. O. Volodkin, "Generation of terahertz surface plasmon polaritons using nondiffractive Bessel beams with orbital angular momentum," *Physical review letters*, vol. 115(16), p. 163901, 2015.

Two-phonon scheme of generating soft terahertz radiation by gold nanobars for detection of hidden objects

K. A. Moldosanov[1], A.V. Postnikov[2], V. M. Lelevkin[1], N. J. Kairyev[1]

[1]Kyrgyz-Russian Slavic University, Bishkek, Kyrgyzstan, altair1964@yandex.ru
[2]University of Lorraine, Institut Jean Barriol, LCP-A2MC, Metz, France

A two-phonon scheme of generating terahertz (THz) photons by gold nanobars (GNBs) is considered. By choosing the dimensions of GNBs, one can provide conditions for conversion of energy of longitudinal phonons into that of THz photons. The prospects of designing the GNBs-based sources of soft THz radiation (with frequencies 0.14; 0.24; 0.41 and 0.70 *THz*) with large beam cross-section (~ 40 *cm* in diameter) are estimated. These sources could be used for detection of hidden objects under the clothing to provide security in public spaces.

The choice of soft THz frequency range is suggested by weak absorption of this radiation by water vapor present in the air, and by its efficient penetration through clothing tissues, thus enabling a good spatial resolution. A sufficiently large concentration of longitudinal phonons within this frequency range, available in GNBs (as well as in bulk gold), seems advantageous for efficient excitation of Fermi electrons, with the subsequent emission of THz photons.

In the present contribution, a novel design for a soft THz radiation source is proposed, based on GNBs being irradiated with microwaves. In order to increase the THz yield, the population of longitudinal phonons is enhanced by microwave irradiation (heating) of GNBs. The use of a large area covered by GNBs densely placed on the substrate, or in the volume of an appropriate matrix, would straightforwardly produce a spatially broad beam of THz radiation.

The physical mechanism of THz generation is that a Fermi electron is excited in the course of absorption of a longitudinal phonon, whereupon the electron relaxes via releasing a softer longitudinal phonon, simultaneously emitting a THz photon. Reference values of the energy difference between the absorbed and the released phonons could be around 0.58 / 0.99 / 1.70 / 2.90 *meV* (based on the features of the density of vibration modes in gold), that would correspond to photon emission at 0.14 / 0.24 / 0.41 / 0.70 *THz*, correspondingly.

The optimal size of GNBs is estimated as 5.3 *nm* × 5.3 *nm* × 1.318 *μm* (see Fig. 1). This choice is fixed by the condition that the relaxation of the excited electron via releasing a longitudinal phonon be blocked, by force of conservation laws for electron / phonon / photon momenta and energies. If fixed on top of, or within, the substrate layer transparent in the THz range, the GNBs can be exposed to microwave radiation of, say, standard frequency of 2.45 *GHz* used in microwave oven. The possible setup is depicted in Fig. 2 (front view) and Fig. 3 (top view). An outer box 1 contains the metal camera 2 within which a substrate 3 with deposited GNBs 4 is placed. A source of electromagnetic radiation (*e.g.*, a magnetron) 5 opens into a waveguide 6. The resonance filter 7 which covers the opening 8 in the box the frequency band of radiation leaving the device. The lens system 9 placed outside the box focuses the THz beam on the inspected object 10.

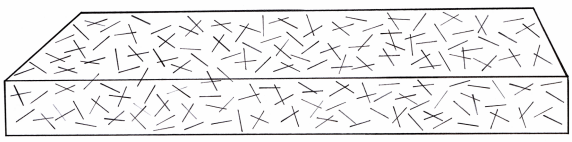

Fig. 1. THz radiation sources in the form of a matrix transparent in THz wavelength range with embedded GNBs

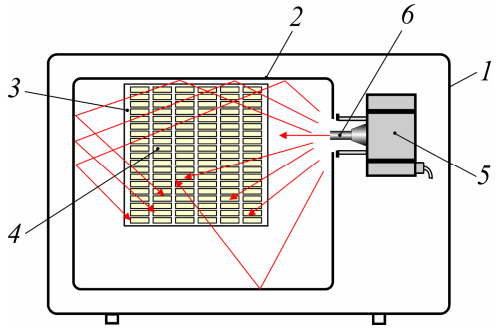

Fig. 2. A possible realization of the GNBs-based soft THz radiation source, front view

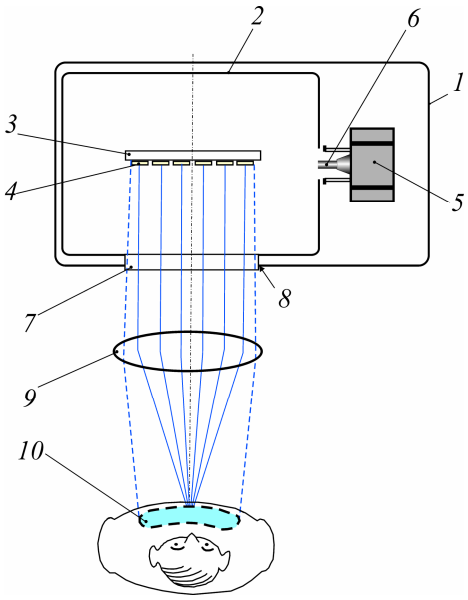

Fig. 3. The same as Fig. 2 in the top view, and the scheme of screening concealed items on the body

Submillimeter wave Tomography and image processing advances : Applications to additive manufacturing quality control

J.B. Perraud[1], A.F Obaton[2], B. Recur[3], H. Balacey[3], J.P. Guillet[1] and P.Mounaix[1]

1 Bordeaux University, IMS, UMR CNRS 5218, 351 cours de la libération 33405 Talence, France

2 Laboratoire National de Métrologie et d'Essais (LNE), Laboratoire Commun de Métrologie (LCM), 1 rue Gaston Boissier, 75015 Paris, France

3 Noctylio SAS, 53 rue Professeur Daguin, 33800 Bordeaux, France

*Corresponding author: Patrick Mounaix patrick.mounaix@u-bordeaux.fr

Additive manufacturing (AM) is an essential tool to make 3D objects having very complex shapes and geometries, unachievable with standard manufacturing approaches. Meanwhile, quality controls of such objects become challenging for both industrials and applications in laboratories due to both their complexity and the materials they are made of. Consequently, we demonstrate that terahertz (THz) imaging and THz tomography can be considered as efficient methods for such object inspection in routine applications. Thus, this paper proposes an experimental study of 3D polymer objects obtained by AM techniques. This approach allows us to characterize defects and to control dimensions by volumetric measurements on 3D data reconstructed by tomography.

Additive manufacturing (AM) methods provide very sophisticated and complex geometries objects without almost material waste. Moreover, these techniques are now appropriate to numbers of materials, including numerous plastics, ceramics, and even metals. However, new defects may occur in the final device with these new techniques so that material quality has to be assessed. Chiefly, physical phenomena related to additive manufacturing processes are complex, including melting, solidification and vaporization, heat and mass transfer. However, every time a new technology emerges, it creates a need for control tools. For example, it is necessary to verify that high-tech components have no defects in order to ensure that they will not become weaker with use. Dimensional measurements of inner structures can also be of paramount importance. Since the position taken by AM in several critical industry sectors (such as aeronautics, aerospace and medical) to produce high-tech parts, it is obvious that both quality control and certification of these parts have to be considered. For example, this principle of fabrication can introduce more defects caused by the bad fusion of a layer and perceived as porosity. The only way to probe and measure complex and/or inner structures manufactured by AM without any damage is to use volumetric Non-Destructive Testing (NDT) techniques. Among these techniques, the only one which both enables defect detection and provides a 3D visualization of inner structures (allowing dimensional measurements) is tomography. In this paper, we demonstrate that TeraHertz (THz) tomography could be an efficient alternative to X-Ray for NDT of AM objects.

Experimental tomography setups:

Continuous wave (CW) THz imaging can be used to obtain 3D reconstruction of an object [1] Tomography algorithm requires that the object under investigation is measured at different viewing angles for obtaining a set of 2D radiographs. In this study, we experiment two setups for measuring such an object acquisition. Both consist of an electronical emitter and receiver equipped with polytetrafluoroethylene (PTFE) lenses to focus the THz radiation on one spot-point of the sample. The object is mounted on a rotational stage to rotate the object which is itself mounted on a pair of horizontal / vertical translation stages. Basically, translating the object relatively to the THz focused beam aims at measuring a 2D radiograph by raster-scanning while iterating this process by moving the rotational stage leads to the acquisition of different angle radiograph views. In all our experiments, the raster-scanning is performed according to the sample dimensions such that it is always included in the radiograph field of view, and 36 radiographs, from angle 0 to 175° with a 5° step, are measured. The first scanner consists of a Gunn Diode emitting 12 mW at 287 GHz and a Schottky diode as receiver. The THz beam is modulated at 1 kHz by a mechanical chopper. The signal is rectified by the ultrafast Schottky diode, and measured by a lock-in amplifier. The lenses used to focus the THz beam have a focal length of 50 mm and a diameter of 50.8 mm, which leads to a waist of approx. 2 mm at Full-Width Half-Maximum (FWHM). The second scanner is based on a chirped signal centered at a certain frequency, which is generated by up-converting a fixed frequency signal. Via a ramp generator and a voltage-controlled oscillator, a signal with swept frequency is generated at approximately 13-18 GHz with a sweep period of 240 µs. A Schottky mixer is employed as heterodyne detector. The lenses used to focus the THz beam have a 200 mm focal length and a diameter of 50.8 mm. 3D tomographic reconstructions from acquired THz radiographs are performed using the Ordered Subsets Convex algorithm (OSC) [2] adapted to THz radiation. We chose this algorithm for its very good results in reconstruction quality with terahertz

waves.is legible. Color figures will be reproduced in black and white.

Samples:

The materials available for 3D printing are numerous and depend on targeted solicitations. There is now a wide variety of material types that are provided in different states (powder, filament, pellets, granules, resin, etc) for many types of printing procedures. Specific materials are also developed for particular systems performing dedicated applications (examples would be the dental, automotive, medical sectors, etc). For example, Nylon, or any Polyamide in general, are commonly provided in powder form with the sintering process or in filament form with the fused deposition modelling process. It is sufficient strong, flexible and durable plastic material that has proved reliable for 3D printing. Acrylonitrile Butadiene Styrene (ABS) is another common plastic used for 3D printing, and is widely used on the entry-level FDM 3D printers in filament form. Polyether ether ketone (PEEK), which is a semi-crystalline thermoplastic with excellent mechanical and chemical resistance properties that are retained to high temperatures. PEEK is considered as an advanced biomaterial used in medical implants. Each material were measured by time domain terahertz spectroscopy to extract their dielectric properties.[3]

Results

Considering spectroscopic analysis, we have imaged in 3D the objects made in thermoplastic materials using the CW-THz scanner with the 287 GHz source. Thanks to an advanced processing sequence [9], going from the 3D tomographic reconstruction to the automated segmentation and meshing of volumes of interest (VOI) we are able to measure the dimensions, analysis the surface, determine the volume morphology and compare the volume with the CAD model developed for 3D printing.

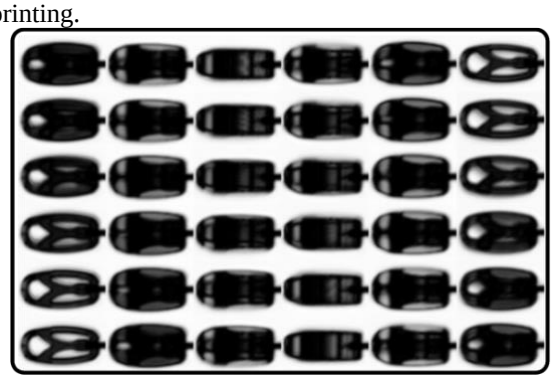

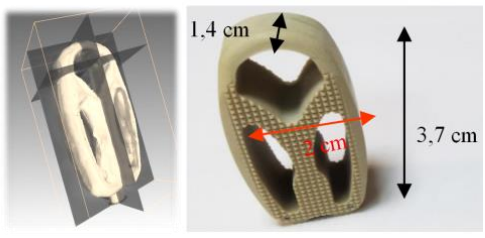

Fig.1 acquisition (set of 36 radiographs) at 287GHz with an angular step of 5°. Down left 3D reconstruction of the object by tomography using the OSC-THz algorithm. Down right Original sample with its dimensions.

For example, Fig.1 shows lumbar interbody 3D reconstruction using the CW scanner equipped with a 287 GHz source. After acquisition of the radiographs of the different samples represented in Fig3. a , tomographic reconstructions are performed in fig3.b . The reconstructed data obtained under different orthoslices reconstructed from the different projections. This rendering allows one to visualize, analyze and measure the sample on surface and in depth. Then visualisation and dimensional measurements can be achieved separately for each Volume Of Interest (VOI), which is particularly useful to analyze correctly the inner structure of an object. We accomplish this analysis by showing how 3D segmentation and 3D rendering [4] can be used as a qualitative and quantitative analysis for inspection

Conclusion

We will demonstrate that several AM objects made of polymers and ceramics could be inspected by THz-TDS and/or 3D THz tomography. Preliminary spectral analysis of the materials used for 3D printing helps at determining the parameters to be applied for efficient 3D tomography. Moreover, for some samples having very specific shapes, time-of-flight THz imaging can be an alternative approach to tomography for 3D inspection. Achieving such NDT requires advanced image processing sequence and algorithms for reconstructing and analysis relevant data extracted from the acquisition. As an example of analysis tools, we have shown that surface and volume analysis can be performed and 3D rendered object dimensions can be compared with original CAD dimensions. Moreover, efficient defect detections can be carried out. Thus, THz imaging is an alternate and complementary technique to the well-known X-Ray tomography which is costly for routine controls.

Aknowledgements.

This study has been carried out with financial support from the French State, managed by the French National Research Agency (ANR) in the frame of "the Investments for the future" Programme IdEx Bordeaux – LAPHIA (ANR-10-IDEX-03-02), and the European Community under the European project FP7 MetrAMMI. We also thank Dassault Aviation for providing the polyamide multivalve sample and Medicrea for providing the lumbar interbody devices

References

[1] B. Recur *et al.*, "Investigation on reconstruction methods applied to 3D terahertz computed tomography," *Opt. Express*, vol. 19, no. 6, p. 5105, 2011.
[2] B. Recur *et al.*, "Ordered subsets convex algorithm for 3D terahertz transmission tomography," *Opt. Express*, vol. 22, no. 19, p. 23299, 2014.

[3] S. F. Busch, M. Weidenbach, M. Fey, F. Schäfer, T. Probst, and M. Koch, “Optical Properties of 3D Printable Plastics in the THz Regime and their Application for 3D Printed THz Optics,” *J. Infrared, Millimeter, Terahertz Waves*, vol. 35, no. 12, pp. 993–997, 2014.
[4] l Balacey H. et al , “Advanced processing sequence for 3D THz imaging,” *EEE Trans. Terahertz Sci. Technol.*, vol. 6, no. 2, pp. 1–8, 2016.

The concept of construction of inspection systems based on quantum-cascade lasers

L.A. Skvortsov [1], P.I. Abramov[1], E.V. Kuznetsov [1], E.M. Maksimov[2], A.P. Shkurinov[3]

[1]JSC "Polyus Research Institute of M.F. Stelmakh", Moscow, Russia, lskvortsov@gmail.com
[2]National Research Nuclear University MEPhI, Moscow, Russia
[3] Lomonosov Moscow State University, Moscow, Russia

Terahertz imaging systems are of particular interest for solving problems related to remote examination of individuals in conditions of dense passenger traffic. The development of compact non-invasive remote detection systems for the detection of hidden explosives is of paramount importance in connection with the increased likelihood of terrorist attacks with their use. In the general case, it is possible to distinguish three most common scenarios for the inspection of individuals (Fig.1).

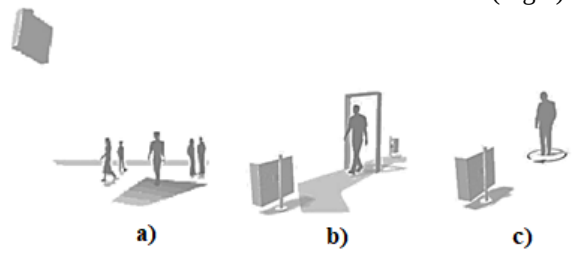

Fig. 1. Possible scenarios for remote screening: a) examination of separately standing persons at a great distance; b) screening of a moving object in conditions of mass passenger traffic simultaneously from the front/side; c) overall (360^0) control.

In general, the concept of construction of inspection systems includes the technique of active formation of spectral images. At the same time, it implies the presence of at least three information channels in different frequency ranges: VIS, MIR and THz. The use of terahertz radiation is due to its ability to penetrate through opaque non-conductive materials, which makes it possible to detect hidden explosives. At the same time, the registration of the radiation scattered by the object in the mid-IR range allows not only to increase the probability of detection of explosives, but also to solve the problem associated with the identification of persons representing a potential terrorist threat, for example, previously had contact with explosives.

The aim of this work is to substantiate the possibility of constructing a terahertz channel of inspection systems based on quantum-cascade lasers for the considered scenarios, due to the innovative technological solutions in the creation of quantum-cascade lasers and advances in the analysis and construction of multi/hyperspectral images.

The active method of forming spectral images in the terahertz spectral range is quite simple. A smoothly (or discretely) tunable laser source with a narrow lasing band (or several sources with a fixed wavelength) affects the inspection object that may contain hidden explosives or their tracks. In this case, the laser tuning region includes the absorption bands of the materials to be detected. The response of the target to the laser action in the form of diffuse scattered/reflected radiation is detected by means of a photodetector device, which can be a special camera, the sensitive element of which is a multi-element array or a single-element receiver (if the scanning facility is capable of scanning). When the wavelength of the laser varies, the ratio between the absorbed and scattered/reflected object is changed by the energy of the laser radiation. For example, increasing the absorption in the target leads to a decrease in the intensity of the scattered light reaching the matrix photodetector device (FPA). This, in turn, leads to a noticeable contrast between the individual parts of the observed scene, for example, between explosive or narcotic substances, clothing and the human body. The thus created hyper/multispectral cube contains a spatially resolved signal as a function of the wavelength of the scattered radiation, which is of particular importance for identifying the object [1, 2]. At the same time, in the THz range, the necessary contrast in the formation of a monochrome image of objects made of conductive materials (metal) is achieved due to the difference in the reflection coefficients.

As possible options for constructing active imaging systems, two basic schemes are usually considered, as shown in Fig. 2.

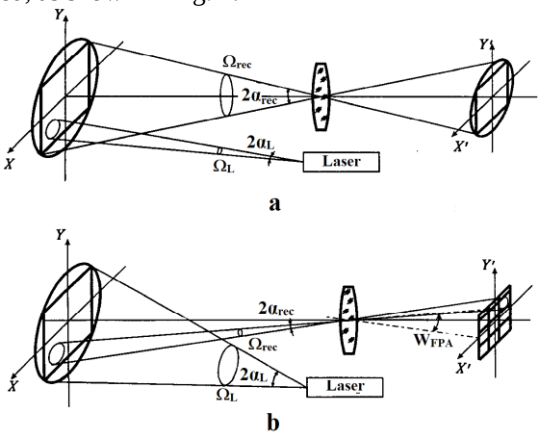

Fig. 2. The main variants laser imaging systems.

In a system of the first type (Fig. 2a), the illumination source has a narrow directivity pattern, and the simultaneous optical receiver is wide, i.e. $\Omega_L << \Omega_{rec}$. The image is formed as a result of sequential scanning of the subject area within the field of view. The receiver registers a continuous signal, modulated in intensity according to the spatial distribution of the reflection/scattering coefficient. From this signal, the video signal following on the monitor is subsequently formed. The size of the element of spatial decomposition of the formed image is determined by the angular divergence of the probing radiation $2\alpha_L$, and the view-

ing angle is determined by the angle of view of the receiving system, equal to $2\alpha_{rec}$ = 2arctg ($d_{rec}/2f'_{ob}$), where d_{rec} is the linear size of the photodetector's area; f'_{ob}, - the focal length of the objective lens of the receiving optical system.

In a system of the second type (Fig. 2b), the illumination source has a wide radiation pattern that illuminates the entire field of view by area *A*, and the receiver is narrow, i.e. $\Omega_L >> \Omega_{rec}$. In such laser imaging systems, there is no scanning, and as a photodetector a matrix Focal Plane Arrays (*FPA*) is used, which directly converts the two-dimensional optical signal into a video signal.

In the table are presented the comparative characteristics of the considered laser imaging systems.

Laser Imaging System	Comparative characteristics
FPA receiver; laser irradiating the entire FOV	High speed, high power laser radiation
Single-element detector; scanning of the laser beam within the inspection area	Low speed; lower laser radiation power

As an example, we give the results of calculating the limiting distance standoff of the laser imaging system used for remote screening in conditions of mass passenger traffic (Fig. 1b).

The basic relationship for calculating the laser radiation power required to provide the detection range L can be represented as:

$$P_L = P_{rec}\frac{4L^2}{\eta D_{rec}^2 \tau_1 \tau_2 \rho} e^{2\alpha L} e^{2\beta d}, \qquad (1)$$

where P_{rec} - power of scattered/reflected radiation, which falls on the sensitive area of the photodetector; τ_1 and τ_2 are the transmittance coefficients of the transmitting and receiving optical systems; D_{rec} - lens diameter of the receiving optical system; α is the coefficient of atmospheric absorption at the wavelength of the laser radiation; β is the absorption coefficient of the barrier material (clothing) behind which the explosive is hidden; ρ is the reflection coefficient of the target; $\eta = P_{scatt}/P_0$ is a coefficient equal to the ratio of the radiation power scattered / reflected by the inspection object P_{scatt} to the total radiation power of the laser P_0 in the object location plane.

To calculate the laser radiation power needed to provide the maximum detection range of L_{max}, it is necessary to substitute P_{rec} in the formula (1) in the form: $P_{rec} = NP_{rec/pix}$. Here $P_{rec/pix} = NEP = F_{thr}$ is the minimum signal that can be detected (the sensitivity threshold of the radiation receiver at the wavelength of the laser), determined by the power equivalent to the noise of the detector (noise equivalent power).

First, we present the results of calculations for a single-element receiver when scanning an inspected object. For numerical calculations, we assume that the area of the field of view in both cases is *A* = 50 cm × 50 cm; the necessary spatial resolution provided by the instantaneous field of view of a single-element detector (the diameter of the laser beam on the target) is *d* = 1 cm; the efficiency of the optical system is $\tau_1 \times \tau_2 = 0.8$; threshold sensitivity of the detector (Golay cell) at the investigated wavelengths of laser radiation $NEP = 1.4 \times 10^{-10}$ W; diameter of the objective lens D_{rec} = 10 cm; the reflection coefficient from the target surface is ~ 10^{-2} [3]. We make an estimate for two cases: in the area of the micro-window of atmospheric transparency, i.e. in the frequency range 3.72 ... 3.74 THz (α = 0.25 m^{-1}) and outside this window at a frequency of 3.66 THz (α = 5.2 m^{-1}). In this case, as an obstacle, let us consider an ordinary woolen sweater of thickness *d* = 0.6 cm, the loss in which is 5.4 dB/mm (β = 6.22 cm-1) [4]. The results of calculations for distances of interest for inspection in conditions of dense passenger traffic are shown in Fig. 3. It should be noted that modern optical-mechanical systems of two-coordinate scanning (galvo scanners) provide a field of view of 25 × 20 degrees, the time of frame formation is ~ 1 *s* and less.

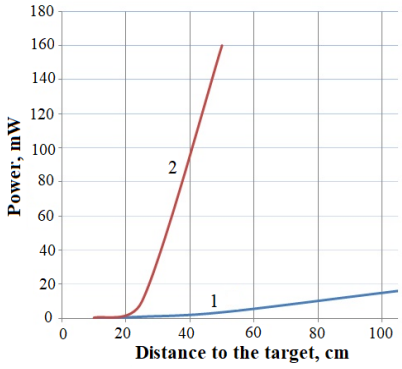

Fig. 3. Dependence of the minimum laser radiation power required to detect TNT at various distances from the entrance window of the receiving channel L_{max} within the micro-window of the atmospheric transparency (curve 1) and outside it (curve 2) at a radiation frequency of 3.66 THz (*P* = 1 atm, *T* = 210 ^{0}C, RH = 30%) in the presence of in both cases obstructions in the form of a wool sweater with a thickness *d* = 0,6 cm, the loss in which is 5,4 dB/mm.

An estimate of the minimum radiation power required to detect a latent explosive using an uncooled bolometric chamber (Figure 2b) at a distance of 50 cm under the same conditions as mentioned above (Figure 3) yields a P_L value of 3 W. In this case, one frame is formed within 0.02 seconds.

Thus, the choice of the scheme for building laser imaging systems for their use in standoff security systems is largely determined by the specific operational task and the capabilities of the existing element base.

References

1. *Skvortsov L. A.* Standoff detection of hidden explosives and cold and fire arms by terahertz time-domain spectroscopy and active spectral imaging //Journal of Applied Spectroscopy, 2014. V. 81. P. 725.

2. *Skvortsov, L.A.* Active spectral imaging for standoff detection of explosives // Quantum Electronics, 2011. V. 41. P. 1051.

3. *Kemp, M.* Millimetre wave and terahertz technology for the detection of concealed treats // Proc. of SPIE, 2006. V. 6402.P. 64020D-1.

4. Federici, J., et al. THz imaging and sensing for security applications—explosives, weapons and drugs // Semiconductor Science and Technology, 2005. V. 20. S266.

Influence of pollution and extraneous inclusions on the scattering of THz radiation by fabric

A. A. Angeluts[1], V. N. Aksenov[1], A. V. Balakin[1], I. A. Ozheredov[1], A. P. Shkurinov[1]

[1]Faculty of Physics M.V.Lomonosov Moscow State University, Moscow, Russia, angeluts@physics.msu.ru

One of the challenges of modern civilization now is the various manifestations of terrorist activity. It is therefore necessary to create different methods of remote diagnostics of dangerous items and substances. One of directions of development of diagnostic methods introduced in recent decades is methods based on the use of Terahertz (THz) radiation.

THz radiation is defined as electromagnetic radiation in the range from 300 GHz to 10 THz (or 30 μm to 1 mm), is of great interest to create diagnostic, measuring and inspection systems. This interest determines firstly by the fact that in recent years, started an intensive development of components for the generation and detection of THz radiation, and secondly, the specific features of the radiation. Among the important properties of this radiation should be noted his non-invasive and non-ionizing nature that allows the use of THz radiation in tasks related to human Diagnostics. In addition, this radiation weakly attenuated by most materials, so such objects, such as cloth, dry wood, paper, plastics are transparent to THz range.

Most often, the diagnostic is to irradiate the THz object of interest by probe beam and then analyze the transmitted, reflected or scattered radiation.

In the present work describes a study, based on analysis of the scattered radiation.

Experimental setup and samples

As the object of the study, tissue samples were selected with TNT traces on their surfaces or that contain a thin metal wire. Such objects simulate a clothes whose surface is contaminated with a hazardous substance or contains elements of electronic devices controlling the explosive device (current leads, antenna elements and so on).

Studies performed with the setup, the simplified diagram is shown in Fig.1. Our experimental setup detailed description can be found in [1]. Radiation with a frequency of 3 THz focused on the surface of the object along normal to its surface. The scattered radiation was collected by a system of parabolic mirrors and detected. Recorded radiation scattered at an angle of approximately 60 degrees from the normal, or 120 degrees from the direction of incidence of the probe beam. This angle allows the detector to avoid specular component of the radiation.

Samples were flaps of cotton fabric. "Contamination" of the sample was carried out by applying TNT solution in acetone to the tissue. Then the sample was dried and weighed.

The sample *Ct14* had a surface contamination density of about 3 mg/cm^2.

The sample *Ct50* had a surface contamination density of 10 mg/cm^2.

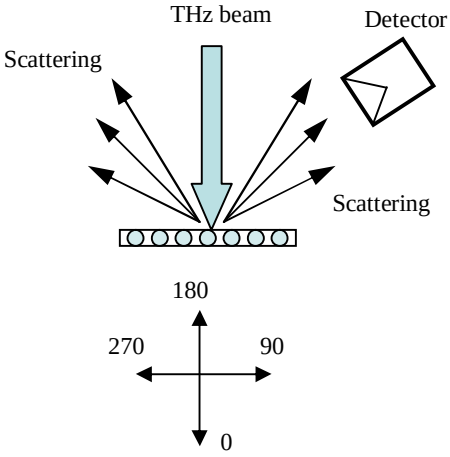

Fig. 1. Scattering experiment schematic

Since no uniform contamination was achieved in the preparation of samples, the above figures only approximately characterize the degree of contamination in the analyzed sample area.

Cm78 sample consisted of a piece of cloth of the same, in which a copper wire of 78 mkm was introduced.

In addition to the samples described above, samples were studied that were copper wires 240 and 78 mkm in diameter. With their help it was conducted an adjustment of the measuring circuit.

Experimental results

Table shows some of the results of the measurements represent the values of ambient signal from different samples. For ease of comparison values of the scattering signal, it was normalized to the value of the scattering signal of pure textiles.

Table . Relative magnitude of scattering for different samples

Sample	Copper wire *f78* mkm	Copper wire *f*240 mkm	Ct14	Ct50	Textile	Cm78
Scattering signal value	5.4	18.3	0.8	0.17-0.58	1	1.75

The signal value for sample *Ct50* shows a spread due to strong heterogeneity of pollution, as when drying solution came the transfer of a substance to the periphery of the sample. So most likely score pollution concentration overstated

As can be seen from the table, tissue contamination leads to suppression of scattering signal in our choice of angle observation from 20% up to 5 times. The magnitude of the suppression is determined by the concentration of the substance in the area under study

The presence of thin conductor reliably detected in tissue. The copper wire with a diameter of 78 mkm sewn into the fabric leads to an increase in the scattered signal by a factor of 1.8.

The scattered signal from a single conductor exceeds the signal from the surface of the cotton fabric from 5 to 20 times, depending on the size of the conductor

The figure 2 shows the result of yet another experiment. Here, the sample *Cm78* moved along the surface plane, simulating the scanning process of the sample. The width of the curve in Fig. 2 is one and a half times smaller than the THz size of the spot on the surface. The "pedestal" of the chart is determined by the scattering from the tissue itself. A slight decrease in the magnitude of the signal at the positions 5 and 6 mm is caused by the destructive interference of the radiation scattered by the tissue and the conductor.

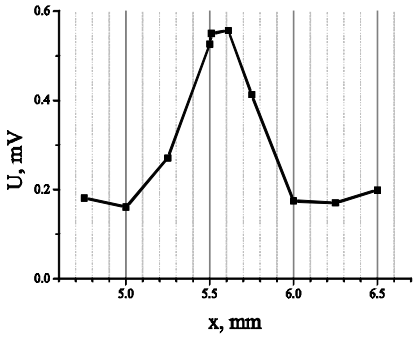

Fig. 2. The result of the movement of Cm78 sample across the probing beam. Detection of hidden wire.

Scattering numerical estimation

A numerical estimate of the scattering was carried out on the simplest model object-an infinite cylinder covered by a layer of an absorbing dielectric [2].. This model most closely describes the textile, which is a set of threads.

In our model for base cylinder, we used parameters of PET (also known as Lavsan) and cotton (see Fig. 3 and 4). The diameter of the threads equals to 100 microns. As a coating, TNT layers of different thicknesses were considered: 0.1, 1 and 10 μm.

Figures 3 and 4 show fragments of the scattering indicatrix for model objects. The angle of 180 degrees corresponds to the direction of backscattering of the incident radiation. On the graphs given, the value of the scattering signal is normalized to the value for the uncoated strand.

Given charts show that the nature of the scattering can vary significantly with increasing thickness of a polluted layer. Strong pollution (layer 10 mkm) leads to the Suppression of scattering that qualitatively corresponds to experiment. Under certain conditions (1 mkm) scattering may even increase. A small contamination (layer 100 nm) changes the magnitude of the signal is less than 10%.

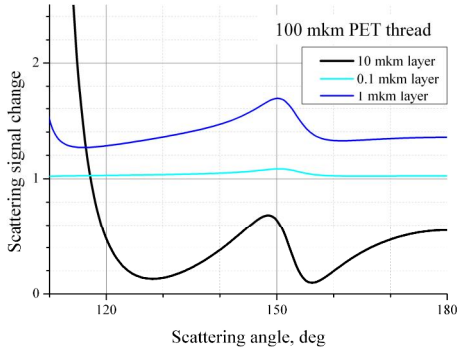

Fig. 3. The change of the scattering indicatrix with the variation in the thickness of the polluting layer on PET thread

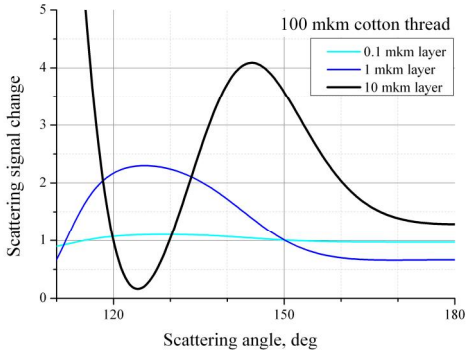

Fig. 4. The change of the scattering indicatrix with the variation in the thickness of the polluting layer on cotton thread

Conclusion

The possibility of detecting current-carrying elements or traces of explosives on the surface of the object by analyzing scattered THz radiation is investigated.

Experimental results and preliminary calculations have shown that the backscattering patterns for textile fibers differ significantly, depending on their material and the presence of contamination on them. This opens up the possibility of developing terahertz-imaging systems in the field of security.

Acknowledgements

This work was supported by the Russian Foundation for Basic Research (project No. 16–29–09593)

References

1. *Aksenov, V. N., Angeluts, A. A., Balakin., A. V. et. al.* Application of a terahertz multi-frequency radiation source based on quantum-cascade lasers for identification of substances basing on the amplitude-spectral analysis of the scattered field // Radiophysics and Quantum Electronics. 2018. V. 60, No. 11. P. 877-888

2. *Kotlar, V. V., Lichmanov, M. A.* Analysis of the diffraction of an electromagnetic wave on an infinite circular cylinder with several homogeneous layers. Computer Optics (*in rus.*). 2002. V. 24. P. 26-23

Svalbard astroclimate research: expedition and first results

Grigoriy Bubnov[1,2], V.F. Vdovin[1,2], P.M. Zemlyanukha[1],V.S. Okunev[1], V.F. Grigor'yev[3]

[1] Institute of Applied Physics RAS, N.Novgorod, Russia, bubnov@ieee.org
[2] Nizhny Novgorod State Technical University n.a. R.E. Alekseev, N.Novgorod, Russia
[3] Polar Geophysical Institute RAS, Murmansk, Russia

Expedition and equipment

This paper deals with the actual results of astroclimate investigations in mm-waveband on Svalbard archipelago. The investigations have begun in June 2018 and are still ongoing. We use the dual-wave radiometric system operating by atmospheric-dip method to estimate an optical depth in 2mm and 3mm atmospheric windows [1]. It has been installed on the polar station of Polar Geophysical Institute near Barentsburg town, Svalbard. (78° 5'42.22"N; 14°12'35.98"E) Remote control system allows to collect data via Internet.

It is also equipped with a makeshift meteostation and anti-icing heater, which is applied in autonomous field experiment for the first time. The meteostation provides a brightness temperature measurement of the sky by IR sensor, apart from typical meteo-data (eg. temperature, pressure, humidity). It allows to define a cloudiness by empiric methodic. Cloudiness calculation methodic is based on work [2,3]. The essence of methodic is to define the difference between real air temperature and brightness temperature by IR-sensor MLX90614. The more this difference is, the less clouds are in air and vice versa; the difference more than 20K corresponds a clear sky conditions, while the difference less than 5K means overcast weather.

As is known, the atmospheric-dip method can't be used in overcast conditions. The new data processing method, which is firstly applied in 2018 [4], allows to save some part of data, measured in overcast conditions. Resulting optical depth includes absorption in stratus clouds as well. Picture 1 shows 5-day record of optical depth τ (Nep) vs temperature difference dT (K). Increasing difference dT between physical air temperature and IR brightness temperature means more clear sky conditions in July 16. This is also accompanied by decreasing mm-wave Optical depth values.

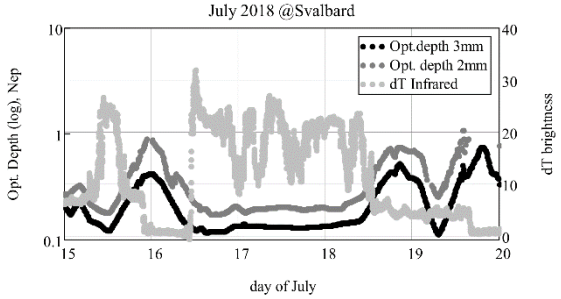

Fig. 1. MM-wave optical depth (log scale) vs temperature difference by IR sensor.

Optical depth and PWV

One of the most important result is an optical depth statistic, which is measured by our "MIAP-2" setup. A cumulative distribution shown below are representing the month-averaged optical depth values. We can characterize the astroclimate on Svalbard as poor for mm-wave observations in Summer period.

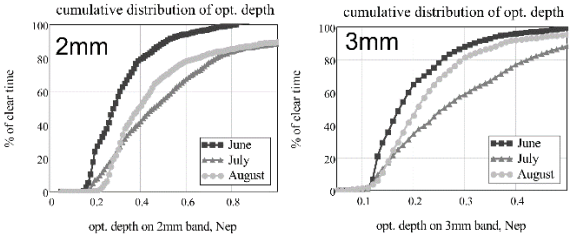

Fig. 2. Cumulative distribution of Optical depth in 2mm and 3mm atmospheric windows in Summer.

Such high values of optical depth are mostly due to high air humidity values and cloudiness. It is usually correlated in time (see pic.3).

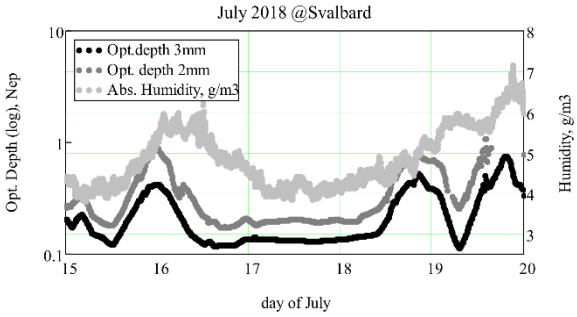

Fig. 3. MM-wave optical depth (log scale) vs Absolute humidity.

Since 2012 we have provided s several expeditions on astroclimate research, so now we can compare these places by month-median values (see pic. 4). Current Svalbard measurements are not promising, but the full-year result remains to be seen.

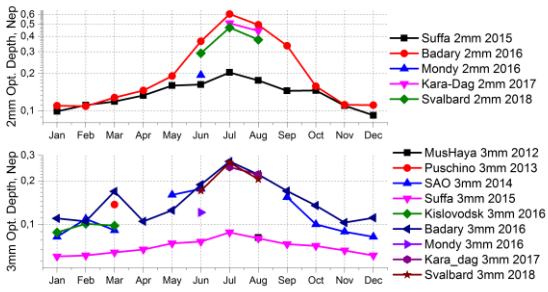

Fig. 4. MM-wave optical depth (log scale) in different places over the Eastern Hemisphere measured by MIAP-2 setup.

Knowing the Optical depth, it is easy to calculate the PWV (mm) [1,4]. The PWV values obtained below (Fig.5) includes a condensed water as well as water vapor by MIAP-2, but not for measurements in [5]. The

data given in [5] obtained by Bouger method. It means that precipitable water is measured only in sunny days, and thus, it has a few statistics. It is the reason why these values are about 80% higher than presented in [5].

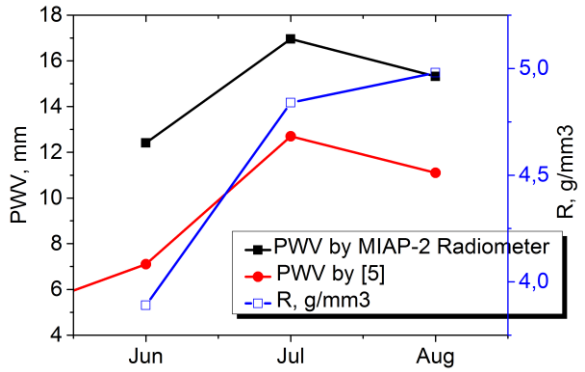

Fig. 5. Precipitable water vapor and relative humidity on Svalbard in Summer.

Using the data obtained by MLX90614 IR sensor in meteostation, it is possible to calculate the cloudiness statistics. The reference points of temperature difference were chosen as: ≤18K for Overcast, from 18 to 27K – Cloudy and upper than 27 - for Clear sky conditions. The obtained results are generally consistent with meteorological observations [6].

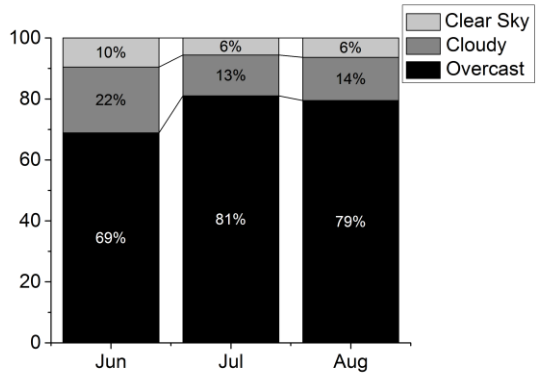

Fig. 6. Cloud statistics by IR sensor.

In **conclusion** we have to characterize Svalbard as non-suitable for mm-wave radioastronomy at least in summer period. The winter period approaching soon and inspires a hope to be much better due to low temperatures. Another important result is a good reliability of equipment: it routinely works for 3 months without any assistance. The makeshift Arduino-based meteostation gives a satisfying result. We will continue measurements in Barentsburg till June 2019 to close the year-cycle.

Acknowledgements

This work has been made with particularly financial support from IEEE APS Eugene F. Knott Memorial Doctoral Research Grant, as well as the scholarship issued by RF President [СП-5103.2018.3.]. The authors would like to grateful Oleg Kutkov and Sergey Nazarov from Krimean Astrophysical Observatory for helpful advice [3] and S.M. Sakerin, D.M. Kabanov from Institute of Atmospheric Optics of RAS for provided data. Special thanks for Barentsburg staff Yu.A. Kvashnin, V.G. Kuleshov and J.D. Mishakova for help in expedition.

References

1. *V. I. Nosov, O. S. Bolshakov et al.* A dual-wave atmosphere transparency radiometer of the millimeter wave range. // Instruments and Experimental Techniques. May 2016, Vol 59, Issue 3, pp 374-380. DOI: 10.1134/S0020441216020111

2. *Nazarov, S. V., Kutkov, O. E.* Infrared cloud sensor at CrAO // Proc. of 47th International student scientific conference, Yekaterinburg. 2018. p.261. ISBN:978-5-7996-2283-1

3. [online] http://olegkutkov.me/2017/08/10/mlx90614-raspberry

4. *G.M. Bubnov, V.F. Vdovin, P.M. Zemlyanukha and I.I. Zinchenko.* A refined method of the data processing for astroclimate measurements in mm-waves. // Proc. of 29th IEEE International Symposium on Space Terahertz Technology, Pasadena, California, USA, March 26-28, 2018.

5. *S.M. Sakerin, D.M. Kabanov et al.* Generalization of Results of Atmospheric Aerosol Optical Depth Measurements on Spitsbergen Archipelago in 2011–2016 // Atmospheric and Oceanic Optics, 2018, Vol. 31, No. 2, pp. 163–170.

6. [online] www.meteoblue.com

Microstructured sapphire shaped crystals for anitiresonant and bandgap terahertz waveguiding

G.M. Katyba[1,2,*], N.V. Chernomyrdin[2,3] K.I. Zaytsev[2,3], and V.N. Kurlov[1,2]

[1] Institute of Solid State Physics of the Russian Academy of Sciences, Chernogolovka 142432, Russia
[2] Bauman Moscow State Technical University, Moscow 105005, Russia
[3] Prokhorov General Physics Institute of the Russian Academy of Sciences, Moscow 119991, Russia
*E-mail: katyba_gm@issp.ac.ru

Terahertz (THz) radiation offers significant scientific and technological applications in many fields [1]; among them: security systems [2,3], medical diagnosis [4–7], non-destructive sensing of materials [8], etc. Nevertheless, the use of THz technologies in these demanding applications is limited by the absence of commercially-available THz waveguides and endoscopic systems, which are capable for the THz wave delivery to hardly acceptable objects with small dispersion and loss.

Recently, several types of THz waveguide have been developed relying on various physical principles. The oldest THz waveguides are based on the hollow-core metal or metal-dielectric tubes [9]. Such waveguides are characterized by relatively low propagation losses, but also feature significant dispersions. In turn, the THz waveguides based on plasmonic structures [10], such as single or dual metal wires, metal plates and ribbons, are convenient in manufacturing and characterized with small dispersion, low propagation and bending losses; however, they are plagued by low coupling efficiency and handling problem, which prevent a practical implementation of these waveguides. Significant progress in the THz waveguiding is associated with numerous developments of flexible polymer microstructured waveguide with different cross-section geometry. These waveguides realize either the anti-resonant reflecting optical waveguiding (ARROW) principle [11], or the Bragg guidance by a photonic crystal (PC) cross-section [12,13]. In such waveguides, the dispersion could be managed and the loses could be minimized by optimizing the geometry of a waveguide cross-section; however, such waveguide remain very sensitive to external perturbations and bending and, thus, are not capable for operation at high temperatures and pressures, since most of the polymers possess relatively low melting temperature and radiation resistance.

An alternative approach would be to use the THz waveguide and fibers, based on the crystalline material, which physical and mechanical characteristics are mainly independent from temperatures/pressures environments and from measurement conditions. In order to answer the challenging problem posed by the THz waveguiding, in our research work, we developed several types of THz waveguides based on the sapphire shaped crystal. These waveguide combines unique physical properties of sapphire (it is transparent in a broad range of electromagnetic spectrum, spanning the ultraviolet, visible and infrared bands; it has high hardness, melting point, thermal conductivity, chemical resistance, tensile strength and thermal shock resistance) and advantages of the edge-defined film-fed growth (EFG) technique (it yields fabrication of the sapphire shaped crystals with a pre-determined cross-section geometry, and an impressive volumetric and surface quality of the shaped crystal) [14-16]. We designed and fabricated two microstructured hollow-core sapphire THz waveguides with different cross-section geometries see Fig. 1. [17,18]. We have combined numerical analysis, using *Lumerical mode solution*, and experimental studies, using the transmission-mode THz time-domain spectroscopy, in order to demonstrate that both of the developed waveguides demonstrate advanced optical performance.

The first sapphire THz waveguide (see Fig. 1 (a)) possesses 7 hollow channels in its cross-section – i.e. 1 core channel and 6 cladding channels [17]. The diameter of each channel is 2.5 mm, while the outer diameter of the waveguide is 12.0 mm. These hollow channels form a hexagonal lattice in the waveguide cross-section with the period of 3.0 mm. Owing to rather low number of the cladding channels in the waveguide cross-section, it realizes mainly the ARROW principle of electromagnetic waveguidance. It yields guidance of THz radiation in a multimode regime with a small dispersion in the frequency range of 1.00 to 1.55 THz and the lowest propagation loss of 2.0 dB/m at 1.45 THz.

The second sapphire THz waveguide (see Fig 1 (b)) possesses the outer diameter of 24.0 mm and much more delicate PC cross-section [18]. This waveguide contains a large hollow core with the diameter of 7.15 mm, as well as 30 channels of the PC cladding, featuring the diameters of 1.6 mm and forming a hexagonal PC lattice with the period of 2.8 mm. For this shaped crystal, we observed an efficient THz waveguidance with a small dispersion in the frequency range of 0.65–1.2 THz and the lowest propagation loss of 0.01–0.03 dB/cm around 1.2 THz. We should mention that the THz radiation propagates throw this waveguide in an effectively two-mode regime; thus, leading to the intermodal interference phenomenon. In Ref. [18], we proposed an analytic model describing this two-mode guidance based on a coherent superposition of the amplitude of the two interfering waves featuring distinct amplitudes and phases. This two-mode guidance can be useful in the intrawaveguide interferometric sensing.

Finally, In Ref. [18], we demonstrated an opportunity for using the two-mode sapphire waveguide from Fig. 1 (b) in a high-temperature THz intrawaveguide interferometry of sodium nitrite ($NaNO_2$) film melts. In our experiment, the sapphire waveguide was

used simultaneously as a cuvette for analyte and as a THz waveguide. During the THz wave propagation throw this waveguide, the effect of intermodal beating occurs. The interference pattern behind the output end of the waveguide forms both in the frequency domain and the spatial domain. This interference pattern strongly depends on the refractive index of the analyte placed in the waveguide hollow core. In this way, we can register the phase transitions of the $NaNO_2$ by measuring the interference pattern at different temperatures in the range of 170 to 300°C. The sharpest change in the interference pattern corresponds to the melting temperature of $NaNO_2$ film. The detailed description of this experiment is presented in Ref. [18].

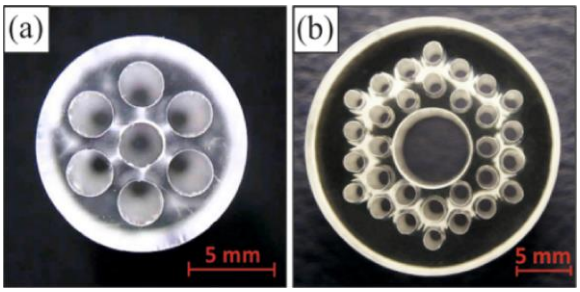

Figure 1. Cross-sections of two EFG-grown microstructured sapphire THz waveguides: (a) an ARROW multimode waveguide with 7 hollow channels [13]; (b) an effectively-two-mode PC waveguide with 31 hollow channels [14].

This work was supported by the Russian Foundation for Basic Research (RFBR), Projects # 17-08-00803 and 17-38-80057.

References

1. *Lee, Y.-S. Principles of Terahertz Science and Technology* // Springer, New York, NY, USA, 2009.

2. *Dolganova, I.N., Zaytsev, K.I., Metelkina, A.A. Karasik, V.E., Yurchenko, S.O.*, A hybrid continuous-wave tehahertz imaging system // Review of Scientific Instruments, 2015, V. 86, No. 11, P. 113704.

3. *Dolganova, I.N., Zaytsev, K.I., Yurchenko, S.O.,Karasik, V.E., Tuchin V.V.*, The Role of Scattering in Quasi-Ordered Structures for Terahertz Imaging: Local Order Can Increase an Image Quality // IEEE Transactions on Terahertz science and Technology, 2018, V. 8, No.4, PP. 403–409.

4. *Zaytsev, K.I., Kudrin, K.G., Karasik, V.E, Reshetov, I.V., Yurchenko, S.O.*, In vivo terahertz spectroscopy of pigmentary skin nevi: Pilot study of non-invasive early diagnosis of dysplasia // Applied Physics Letters, 2015, V. 106, P. 053702.

5. *Zaytsev, K.I., Gavdush, A.A., Chernomyrdin, N.V., Yurchenko, S.O.*, Highly Accurate in Vivo Terahertz Spectroscopy of Healthy Skin: Variation of Refractive Index and Absorption Coefficient Along the Human Body // IEEE Transactions on Terahertz science and Technology, 2015, V. 5, No.5, P. 817–827.

6. *Chernomyrdin, N.V. Kucheryavenko, A.S. Kolontaeva, G.S., Katyba, G.M., Dolganova, I.N., Karalkin, P.A., Ponomarev, D.S., Kurlov, V.N., Reshetov, I.V., Skorobogatiy, M. , Tuchin, V.V., Zaytsev, K.I.*, Reflection-mode continuous-wave 0.15lambda-resolution terahertz solid immersion microscopy of soft biological tissues // Applied Physics Letters, 2018, V.113, No. 11, P. 111102.

7. *Chernomyrdin, V.N., Gavdush; A.A., Beshplav, S.-I.T.,Malakhov, K.M., Kucheryavenko, A.S., Katyba, G.M., Dolganova, I.N., Goryaynov, S.A., Karasik, V.E., Spektor, I.E., Kurlov, V.N., Yurchenko,S.O., Komandin,G.A., Potapov,A.A., Tuchin,V.V., Zaytsev,K.I.*, In vitro terahertz spectroscopy of gelatin-embedded human brain tumors: a pilot study // Proceedings of SPIE, 2018, V. 10716, P. 107160S

8. *Yakovlev, E.V., Zaytsev, K.I., Dolganova, I.N., Yurchenko, S.O.* Non-Destructive Evaluation of Polymer Composite Materials at the Manufacturing Stage Using Terahertz Pulsed Spectroscopy // IEEE Transactions on Terahertz science and Technology, 2015, V.5, No.5, P. 810–816.

9. *Bowden, B., Harrington, J, A ,Mitrohanov O.*, Fabrication of terahertz hollow-glass metallic waveguides with inner dielectric coatings // Journal of Applied Physics, 2008. V. 93, P. 093110.

10. *Wang, K., Mittleman D.M.*, Metal wires for terahertz wave guiding // Nature, 2004, V. 432, P. 376.

11. *Chen, L.-J., Chen, H-.W., Kao, T.-F., Lu, J.-Y., Sun, C.-K.*, Low-loss subwavelength plastic fiber for terahertz waveguiding // Optics Express, 2006, V. 31, No. 3, P. 308–310.

11. *Hassani, A., Dupuis, A. and Skorobogatiy, M.*, Low loss porous terahertz fibers containing multiple subwavelength holes // Applied Physics Letters, 2008, V. 92, P. 071101.

13. *Ma, T., Guerboukha, H., Girard, M., Squires, A., Lewis, R., Skorobogatiy, M.*, 3D Printed Hollow-Core Terahertz Optical Waveguides with Hyperuniform Disordered Dielectric Reflectors // Advanced Optical Materials, 2016, V. 4, No.12, P. 2085.

14. *Antonov, P.I., Kurlov, V.N.*, A review of developments in shaped crystal growth of sapphire by the Stepanov and related techniques // Progress in Crystal Growth and Characterization of Materials, 2002, V. 44, No.2, P. 63–122.

15. *Abrosimov, N.V., Kurlov, V.N., Rossolenko, S.N.*, Automated control of czochralski and shaped crystal growth processes using weighing techniques // Progress in Crystal Growth and Characterization of Materials, 2003, V. 46, No. 1–2, P. 1–57.

16. Katyba, G.M., Zaytsev, K.I., Dolganova, I.N., Shikunova, I.A., Chernomyrdin, N.V., Yurchenko, S.O., Komandin, G.A., Reshotov, I.V., Nesvizhevsky, V.V. and Kurlov, V.N., Sapphire shaped crystal for waveguiding, sensing and exposure applications // Progress in Crystal Growth and Characterization of Materials (accepted, 2018)

17. *Zaytsev K.I., Katyba G.M., Kurlov V.N., Shikunova I.A., Karasik V.E., Yurchenko S.O.*, Terahertz Photonic Crystal Waveguides Based on Sapphire Shaped Crystals // IEEE Transactions on Terahertz science and Technology, 2016. V.6, No. 4, P. 576–582.

18. *Katyba G.M., Zaytsev K.I., Chernomyrdin N.V. Shikunova I.A., Komandin G.A., Anzin V.B., Lebedev S.P., Spektor I.E., Karasik V.E., Yurchenko S.O., Reshetov I.V., Skorobogatiy M., Kurlov V.N. and Skorobogatiy M.*, Sapphire photonic crystal waveguide for terahertz sensing in aggressive environments // Advanced Optics Materials, 2018, DOI: 10.1002/adom.201800573.

Investigation of the influence of the location on the rate of Sub THz space communications channels

I.V. Lesnov[1,2], G. M. Bubnov[1,2], V. F. Vdovin[1,2],

[1]Federal Research Center Institute of Applied Physics of the Russian Academy of Sciences, Nizhniy Novgorod, Russia, ss18f@mail.ru

[2]Nizhny Novgorod State Technical University n.a. R.E. Alekseev, Nizhniy Novgorod, Russia

The need to increase a rate of long-distance space links, in particular, supposed to be developed for communication with the Martian and longer space missions, as well as the space observatory Millimetron, leads to the development of a subterahertz frequency band for this purpose [1]. However, it is known that the terahertz waveband has a noticeable level of absorption in the atmosphere, which appreciably reduces the effect of increasing the channel capacity due to the expansion of the transmission band and the working frequency. Now the main long-distance space communication stations in Russia working in the centimeter range are located in Ussuriysk, Evpatoria, Kalyazin and Bear Lake, while the altitude above the sea level is very small and the absorption of mm and sub-mm waves is significant. Astronomical observations on sub THz waves are usually carried out in high-altitude conditions (over 2500 m), which significantly reduces the effect of the atmosphere on the propagation of these waves. The purpose of this work was to investigate the dependence of the capacity of long-range space communication channels on sub-THz waves from the location of the ground-based communication antenna. To compare the existing sites used for space communications now and prospective ones located in the mountains. Our purpose is to estimate a THz-data link with the best cooled receiver in the "Earth-Space" configuration.

The main parameter influencing the estimation is the data link availability in a specific region and amount of transmitted-received information throughout a year. The location of some stations is shown in Table 1.

Table 1

Object name	Geographic coordinates	Altitude above sea level, m
Suffa Radio Observatory on the Suffa plateau, Uzbekistan.	39°37′N 68°27′E	2335
East Center for Deep Space Communications, Galenki (Ussuriysk), Russia.	44°00′58″N 131°45′25″E	93
Center for Distant Space Communication (Yevpatoria, Crimea)	45°11'20.7"N 33°11'14.5"E	15

When calculating the capacity of the channel, they relied on the method described in [2] with the only difference that the attenuation of the atmosphere decreased with altitude.

At the initial stage, the program reads from the file the altitude profiles of pressure, temperature and humidity obtained by meteorological observations. These data are available at all major weather stations and are posted on the Internet two or four times a day [3]. Tabular data from the file is subjected to piecewise linear interpolation, are given in mutual correspondence of dimensions, and the measurement limits are limited by the altitude of the weather station above sea level h_min and the altitude of the probe h_max (usually 20-30km). The main stage of the program is integration of attenuation coefficients in oxygen and water vapor in height at a given frequency:

$$\tau_{oxygen}(f) = \int_{h\_min}^{h\_max} A_{oxygen}(f, P(h), W(h), T(h))dh$$

$$\tau_{water}(f) = \int_{h\_min}^{h\_max} A_{water}(f, P(h), W(h), T(h))dh$$

where: τ_{oxygen} integral attenuation in oxygen at the zenith, Np τ_{water} – integral attenuation in water vapor at the zenith, Np *h_min u h_max* – range of probe height, km A_{oxygen} – stationary absorption in oxygen, Np/km A_{water} – absorption in stationary conditions in water vapor, Np/km *f* – frequency, GHz *P(h)* – altitude pressure profile, mbar *W(h)* – altitude humidity profile, g/m^3 *T(h)* – altitude profile of temperature, K *h* – height, km.

The result is a spectrum of integral attenuation in the atmosphere. Substituting the center frequencies, the integral weakening of the corresponding transparency windows is calculated. The functions *Aoxygen* (f, P, W, T) and *Awater* (f, P, W, T) are internal functions of the MPM Liebe basic program and determine the linear absorption (He / km) under steady-state conditions, i.e. on a horizontal track. By integrating them with the corresponding profiles, we obtain an integral attenuation on the vertical path (He). The total absorption is the arithmetic sum of the absorptions in oxygen and in water vapor, and the conversion of the quantities in neperes into decibels is carried out by multiplying by a constant of 8.68.

Changing the height h_min in the integrals, we calculate the integral attenuation from the corresponding height, i.e. if the ground station were located at an altitude h_min taking into account the current atmospheric profile.

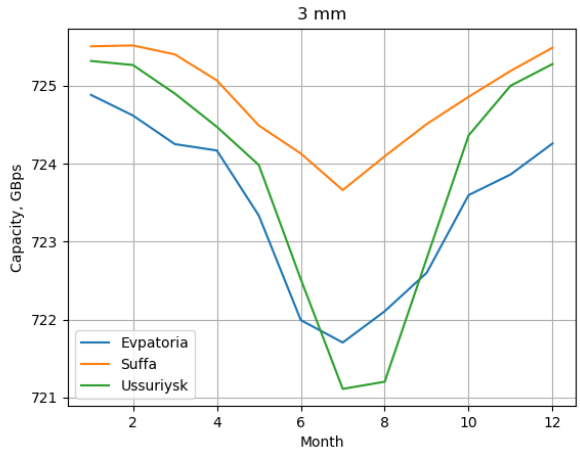

Fig. 1. Estimated THz-link budget for 3mm wave length during a year with cryogenically cooled receiver

Figure 1 showing the variation of the channel capacity for 3mm wavelengths. The calculation was carried out for the following parameters: the width of the window-band is 50GHz, the physical temperature of the receiver is 4K, the equivalent receiver noise temperature is 100K [4], the direction of transmission is zenith.

The total amount of information available for transmission for the year will be: Evpatoria 22502*10^{15}bytes, Ussuriysk 22514.670*10^{15}bytes, Suffa 22545 10^{15}bytes. Expectedly there is a failure in the summer months due to increased humidity, but it is not dramatic in comparison to the three locations. In the annual cycle, the difference is also less than 1%. Certainly when the space port of the channel is located far from the zenith affect of the atmosphere increase. For shorter SubTHz atmospheric windows of transparency (2, 1.3 and 0.8 mm) too. The work was supported by the IAP RAS state program (project No. 0035-2014-0021)

References

1. *V. F. Vdovin, V. G. Grachev, S. Yu. Dryagin, A. I. Eliseev, R. K. Kamaletdinov, D. V. Korotaev, I. V. Lesnov, M. A. Mansfeld, E. L. Pevzner, V. G. Perminov, A. M. Pilipenko, B. D. Sapozhnikov†, and V. P. Saurin* Cryogenically Cooled Low-Noise Amplifier for Radio-Astronomical Observations and Centimeter-Wave Deep-Space Communications Systems// Astrophysical Bulletin Vol. 71, No. 1, 2016

2. *G.M.* Bubnov, *I.V. Lesnov and V.F. Vdovin* Data rates of SubTHz wireless telecommunication channels // EPJ Web of Conferences 2017. 149, №02012 p. 2

3. *H. Liebe, P. Rosenkranz and G. Hufford* Atmospheric 60-GHz oxygen spectrum: New laboratory measurments and line parameters // J. Quant. Spectrosc. Radiat. Transfer 1992, vol. 48, no. 5, pp. 629-43,

4. *Koshelets, V., Birk, M., Boersma, D., et al*. Integrated Submm Wave Receiver: Development and Applications in the book “Nanoscience Frontiers - Funda-mentals of Superconducting Electronics”, Springer Se-ries: Nanoscience and Technology 35372, pp. 263-296, Editor: Anatolie Sidorenko, 2011

Detection and Identification of a Substance with an Inhomogeneous Surface Using the Effective Time-Dependent THz Spectroscopy Method and Emission Frequency Up-Conversion

Vyacheslav A. Trofimov[1,2], Svetlana A. Varentsova[2], YongqiangYang[1]

[1]South China University of Technology, Guangzhou, China, vatro@cs.msu.ru
[2]M.V. Lomonosov Moscow State University, Moscow, Russian Federation

Currently, the THz radiation is actively applied for solving security and anti-terrorism problems [1], [2]. In most THz TDS setups, the substance identification occurs based on comparison of the absorption frequencies of a substance under investigation with a set of known absorption frequencies from a database (we call it as the standard THz TDS method). However, this technology has certain limitations.

It is well-known that surface roughness can lead to scattering and modulating of the spectrum, which complicates the identification [3], [4]. To overcome this problem, in [3] it was shown that by summing and averaging multiple measurements over a sample area the scattering effect can be effectively decreased. In [4] the authors proposed for the same purpose to increase the number of viewing angles. However, they can reliably identify only one absorption frequency with maximal spectral amplitude.

Unlike the methods mentioned above, in the discussed method we use only one THz signal reflected from the substance with inhomogeneous surface but measured in the long time interval duration 180-200 ps. This duration allows registering not only the main reflected THz pulse, but also several sub-pulses following it, which are due to the reflectance from the inner surfaces of the sample. These sub-pulses also contain information about spectral characteristics of the substance and can be used for the identification. In addition, we do not apply averaging of measurements over viewing angles and the sample area in order to reduce the scattering effects.

As an example of identification, we use the THz signal duration 180 ps reflected from the PWM C4 explosive (90 % RDX, 10 % plasticizer) with a rough surface grit 40 (signal PWM_40 for brevity). The signal contains the pronounced main pulse reflected from the outer surface of the sample, the first sub-pulse reflected from the inner surface, and the sub-pulses with significantly less amplitude due to multiple reflections from the inner surfaces. The Fourier spectrum of the PWM_40 main pulse is shown in Fig. 1 (a) together with that of the smooth PWM for comparison.

The spectral properties of the PWM_40 main pulse are distorted by the influence of the inhomogeneous surface (a) so that the standard THz TDS method is inefficient for identification. In the PWM_40 spectrum (a) there is a single minimum at the frequency ν=0.88 THz in the frequency range ν=[0, 1.8] THz, which is close to RDX absorption frequency ν=0.82 THz. In the frequency range ν=[1.8, 4.0] THz there are minima at the frequencies ν= 1.92, 2.24, 3.0 THz , which are close or equal to the RDX absorption frequencies ν= 1.95, 2.19, 3.0 THz [2].

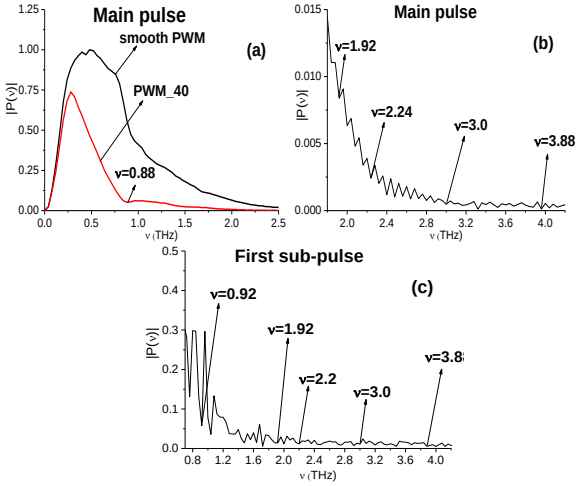

Fig. 1. Fourier spectrum of the main pulse of the PWM_40 and smooth PWM signals in the frequency ranges ν=[0.0, 2.5] THz (a), [1.8, 4.2] THz (b), spectrum of the PWM_40 first sub-pulse in the frequency range ν=[0.8, 4.2] THz (c).

The spectrum of the PWM_40 first sub-pulse contains minima at the frequencies ν= 0.92, 1.92, 2.2. 3.0 THz (c), that are close to the absorption frequencies of explosive RDX ν=0.82, 1.95, 2.19, 3.0 THz ([2]). And the spectrum of the remote part of the PWM_40 signal corresponding to the time interval t=[70, 170] ps, contains minima at the frequencies ν = 0.9, 1.96, 2.2, 3.01 THz, which are close to RDX absorption frequencies mentioned above (not shown). Therefore, the sub-pulses also contain information about the substance spectral properties and can be used for identification.

In the current report, the identification is based on the method of spectral dynamics analysis (SDA-method) together with several integral correlation criteria (ICC) [5]. We compare the dynamics of spectral intensity of a substance under analysis with the corresponding dynamics of a standard substance from database at chosen frequencies. To increase the reliability and effectiveness of the identification, we propose to use several ICC's simultaneously in different time intervals, which contain both the main pulse of the reflected THz signal and the following sub-pulses.

In Fig. 2 the evolution of the ICC $CW1_{p,P}$ [5] is calculated for the frequencies ν=0.82 THz (a), (c) and

v =3.0 THz (b), (d) in the time intervals, which contain the main pulse (a), (b) and the first sub-pulse (c), (d) of the PWM_40 signal. In all cases (a)-(d) the frequencies v=0.82, 3.0 THz are detected as RDX absorption frequencies. The same result is valid for the time interval t=[70, 170] ps, containing two other sub-pulses with less amplitude. The ICC $C_{p,P}$ [5] confirms these results.

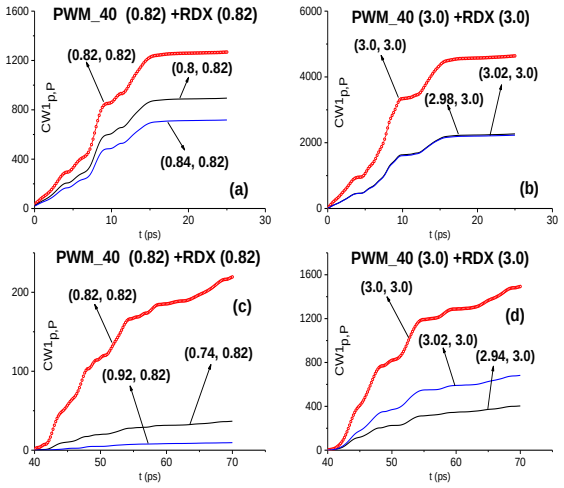

Fig. 2. ICC $CW1_{p,P}(t_n)$ detecting frequencies ν=0.82 THz (a), (c), 3.0 THz (b), (d) in the time intervals t=[0, 30] ps (a), (b), [40, 70] ps (c), (d).

Another promising approach for the substance detection and identification is related to the frequency up-conversion based on a broadband THz pulse. The THz pulse induces high energy level excitation of molecules due to essential non-stationary medium response. This leads to the substance emission at frequencies, which are absent in the incident pulse spectrum. Earlier the frequency up-conversion and the appearance of the doubled current frequency in the THz signals transmitted through or reflected from the medium without and with covering were demonstrated using a mathematical modelling in [6]. The mathematical model is based on the 1D Maxwell-Bloch equations and density matrix formalism. In the current report, we investigate the possible manifestation of the frequency-up conversion in the THz signal PWM_40 reflected from the substance with a rough surface.

Note that the spectra of the PWM_40 main pulse Fig. 1 (b) and the first sub-pulse Fig. 1 (c) contain minima at the frequency ν= 3.88 THz, which is close to the doubled frequency ν= 1.92·2 THz. The same is observed in the PWM_40 spectrum corresponding to the time interval t=[70, 170] ps.

In Fig. 3 the evolution of the ICC $CW1_{p,P}$ calculated for the frequency pair v=(3.88, 1.92) THz is shown in the time intervals containing the PWM_40 main pulse (a) and the first sub-pulse (b). In both cases, the frequency v = 3.88 THz is detected as the doubled RDX frequency in the reflected signal PWM_40. The ICC $C_{p,P}$ [5] also confirms these results.

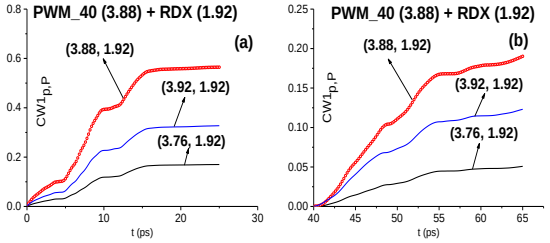

Fig. 3. ICC $CW1_{p,P}$ calculated for the PWM_40 signal at the doubled frequency ν=3.88 THz and the standard signal RDX_Air at the frequency ν=1.92 THz in the time intervals t=[0,25] ps (a), [40, 65] ps (b).

We propose an effective time-dependent THz spectroscopy method, which allows detecting and identifying a substance with inhomogeneous surface using only one long-duration reflected THz signal without averaging of the measured THz signals over the viewing angles and scanning over the surface area. For successful analysis and identification, the registered THz signal must contain both the main reflected THz pulse and several sub-pulses. This feature of the method significantly increases the signal processing speed and allows us to use it in real time.

The possibility for the substance detection and identification using the doubled current frequency is shown with the help of the SDA-method and integral correlation criteria. This result is important for practice, because the frequencies belonging to the high frequency range can be used for the substance detection and identification even in the case when the lower substance absorption frequencies are suppressed by covering or noise influence.

The THz signals reflected from the PWM C4 sample were measured in the Military University of Technology (Warsaw, Poland); THz signal transmitted through the RDX sample - in the Center for Terahertz Research, Rensselaer Polytechnic Institute (NY, USA).

References

1. *Leahy-Hoppa, M. R, Fitch, M. J., Zheng, X., et all.* Wideband terahertz spectroscopy of explosives // Chem. Phys. Lett. 2007. V. 434. P. 227–230.

2. *Liu, H. B., Zhong, H., Karpowicz, N., et all*. THz spectroscopy and imaging for defense and security applications // *Proc. IEEE*. 2007. V. 95, No. 8, P. 1514-1527.

3. *Shen, Y. C., Taday, P. F., Pepper, M*. Elimination of scattering effects in spectral measurement of granulated materials using terahertz pulsed spectroscopy // Appl. Phys. Lett. 2008. V. 92, No. 5. Paper 051103.

4. *Henry, S., Kniffin, G., Schecklman, S., et all.* Measurement and modeling of rough surface effects on terahertz spectroscopy and imaging // Proc. SPIE. 2010. V. 7601. Paper 760108.

5. *Trofimov, V. A., Varentsova, S. A.* Detection and identification of drugs under real conditions by using noisy terahertz broadband pulse // Appl. Opt. 2016. V. 55, No. 33. P. 9605–9618.

6. *Trofimov, V. A., Zakharova, I. G., Zagursky, D. Yu., Varentsova, S. A.* New approach for detection and identification of substances using THz TDS // Proc. SPIE. 2017. V. 10441. Paper 1044107.

Using a Gyrotron as a Source of Modulated Radiation for Data Transmission Systems in the Terahertz Range

A. I. Tsvetkov, A. P. Fokin, A. S. Sedov, M. Yu. Glyavin

Institute of Applied Physics of the Russian Academy of Sciences, Nizhny Novgorod, Russia, tsvetkov@ipfran.ru

The report describes results of preliminary experiments on using low THz range gyrotron (263 GHz) with medium output power (up to 1 kW in CW mode) as a modulated radiation source for data transmission. It was demonstrated up to 1.5 Mbit/s data rate. Estimates show that at relatively low costs it is possible to build a gyrotron-based system with a speed of about 1 Gbit/s.

The scientific community is actively discussing the possibility of promotion of data transmission systems in the subterahertz and terahertz frequency range [1−5]. Data transmission in these bands is attractive for a number of reasons including noise immunity and the complexity of signal interception. It should be taken into account that communication links at such high frequencies suffer from attenuation due to polar molecules (mainly H_2O and O_2) in the atmosphere in addition to the large free-space loss. A suitable transmission window of atmospheric transparency can be found at 200 – 300 GHz [6]. Another complication in the implementation of low THz communication systems is the lack of sufficiently powerful radiation sources with flexible capabilities to control the output radiation parameters in these ranges. The experiments described below demonstrate the possibility of using a subterahertz gyrotron for the data transmission.

There are various methods of control of the output power and frequency of electron devices. One of the most used approaches for the gyrotrons is the variation of the potential of one of the electrodes of the magnetron-injection gun (MIG). The most economical way to quickly control the output parameters is to change the voltage at the isolated anode. This fact is caused by small capacity of anode relative to other electrodes and low anode current, so there is no need in complex and expensive power supplies. The change of anode voltage does not alter the electron energy, but only its pitch-factor (ratio of it orbital to longitudinal velocity). Such change of pitch-factor leads to change of the electron beam complex susceptibility and, hence the change of the interaction condition and, finally, frequency and amplitude of the oscillations. To control the gyrotrons output parameters the fast anode voltage control unit was developed that allows gyrotron anode voltage to be modulated in range of 1 kV with slopes better than 1 kV/μs. The active element of the control unit is the tetrode; the voltage drop is proportional to the external control signal. It was demonstrated up to 200 kHz modulation frequency bandwidth in recent experiments.

In the latest experiments performed in the Institute of Applied Physics of the Russian Academy of Sciences (IAP RAS), the gyrotron with an output frequency $f \approx 0.26$ THz was equipped with the PLL system for its frequency stabilization, which was implemented on the basis of the fast variation of the anode potential. Such an approach made it possible to demonstrate the width Δf of a gyrotron radiation spectrum of about 1 Hz, which corresponds to the relative value of $\Delta f / f \approx 3 \cdot 10^{-12}$[7]. The created control system was then used for the experiments described below demonstrating the principle possibility of using a lower terahertz range gyrotron for the information transmission.

This paper reports on experiments in which it was first realized the transmission of an AM modulated radio signal for several meters using a 263 GHz gyrotron [8] radiation with up to 1 kW power as a carrier.

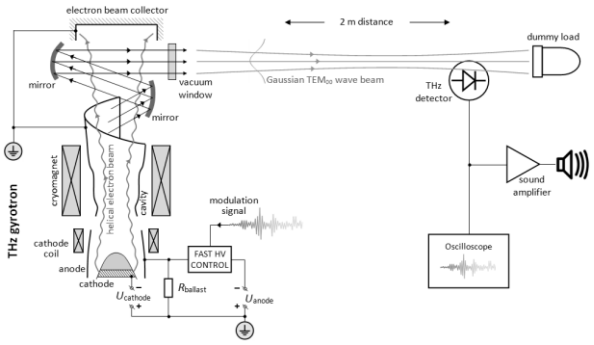

Fig. 1. Diagram of the experimental setup

An ultrafast terahertz (50 GHz – 0.7 THz) detector developed by TeraSense company [9] was used as a radiation receiver and for detecting the AM signal. The detector was installed almost on the path of the gyrotron radiation beam propagation at a distance of several meters from the output vacuum window. The voltage at the anode of the gyrotron was recorded with a NorthStar PVM-5 [10] fast high-voltage probe. Demonstration experiments were carried out at the gyrotron output power level of about 50 W, which in no way limits their generality. Similarly, the parameters of this gyrotron can be controlled at any output power level up to 1 kW.

An audio recorder that provides a level of a modulation signal in the 0 – 10 V range was used in the first experiment. At the same time, the terahertz detector signal was applied to both an oscilloscope and an audio frequency amplifier, followed by output to a loudspeaker. Successful analog transmission of several audio recordings was demonstrated. Fig. 2 shows examples of oscillograms of the corresponding sound signals.

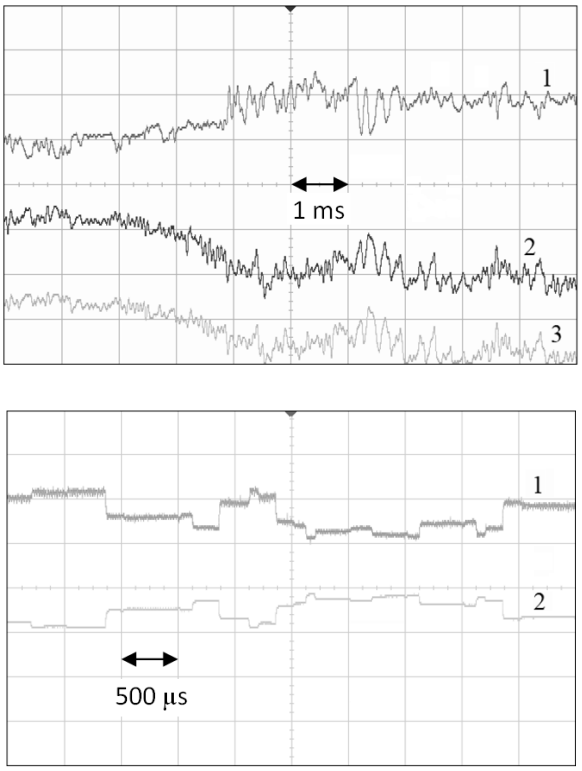

Fig. 2. Top – oscillogramms of the detector signal (1), anode voltage (2), modulation signal of the audio recorder (3); bottom – pseudo-random bit sequence: control (modulating) signal of 33521B generator (1), terahertz detector signal (2).

One can see in Fig. 2 (top) that for some values of the amplitude of the carrier signal the oscilloscope trace obtained from the terahertz detector is distorted with respect to the modulating signal. This is due to the nonlinearity of the slope of the regulating element used in the anode voltage control unit (this effect is especially noticeable near the 0 V control signal) and can in principle be compensated by the choice of a suitable control signal bias.

In the second experiment, the arbitrary waveform generator Agilent 33521B has been used as a source of the control (modulating) signal. It was demonstrated the transmission of a digital signal - a pseudo-random bit sequence (an example of an oscillogram is shown in Fig. 2). In this case, just as in the previous experiment, simple amplitude modulation of the signal was used. Up to a data rate of about 1.5 Mbit/s, the logical levels of the received (detected) signal were resolvable.

The authors believe that the achieved data transfer rate is far from the principal limit and can be increased by decreasing the time constant of the anode power circuit, applying more complex methods for gyrotron output parameters control, using advanced digital signal modulation schemes, increasing the power in the data transmission channel. Simple estimates using the Shannon-Hartley theorem show that it is possible to achieve at least 1 Gbps of channel capacity (under practically the same experimental conditions) by increasing bandwidth of the channel with an improved anode power supply. It is clear that one of the next steps should be a study of the transmission system with respect to various modulation schemes and different symbol rates.

The work was partially supported by the Russian Federation President Grant No. MK-3452.2017.8.

References

1. J. Federici and L. Moeller, “Review of terahertz and subterahertz wireless communications,” Journal of Applied Physics, 107, 111101 (2010).

2. T. Kleine-Ostmann and T. Nagatsuma, “A review on terahertz communications research,” J. Infrared, Millimeter, and Terahertz Waves, 32,143-171 (2011).

3. H.-J. Song and T. Nagatsuma, “Present and future of terahertz communications,” IEEE Trans. Terahertz Science and Technology, 1, 256-263 (2011).

4. T. Nagatsuma et al., “Terahertz wireless communications based on photonics technologies,” Opt. Express, 21, 23736-23747 (2013).

5. T. Kürner and S. Priebe, “Towards THz communications-status in research, standardization and regulation,” J. Infrared, Millimeter, and Terahertz Waves, 35, 53-62

6. V. Petrov, A. Pyattaev, D. Moltchanov and Y. Koucheryavy, “Terahertz band communications: Applications, research challenges, and standardization activities,” in 8th International Congress on Ultra Modern Telecommunications and Control Systems and Workshops (ICUMT), Lisbon, pp. 183-190, Oct. 2016.

7. A. Fokin et al. High-power sub-terahertz source with a record frequency stability at up to 1 Hz // Scientific Reports, 8, 4317 (2018)

8. *M. Glyavin et al.* Experimental tests of 263 GHz gyrotron for spectroscopy applications and diagnostic of various media // Review of Scientific Instruments, 86, No. 5, 054705 (2015)

9. TeraSense: «Ultrafast Terahertz Detectors». URL: http://terasense.com/products/detectors/.

10. North Star High Voltage: «High Voltage Probes». URL: http://www.highvoltageprobes.com/high-voltage-probes